Computers and Fluids 249 (2022) 105688

Contents lists available at ScienceDirect

Computers and Fluids

journal homepage: www.elsevier.com/locate/compfluid

Numerical study of wall shear stress fluctuations and near-wall structures in a square duct at low Reynolds numbers

Rishav Agrawal [a,b,*], Debi Prasad Mishra [c,d], Robert J. Poole [b]

[a] Fluid and Complex Systems Research Centre, Coventry University, Coventry, CV1 5FB, UK
[b] School of Engineering, University of Liverpool, Liverpool L69 3GH, UK
[c] Department of Aerospace Engineering, Indian Institute of Technology Kanpur, Uttar Pradesh 208016, India
[d] Department of Mechanical Engineering, National Institute of Technical Teachers Training and Research, Kolkata 700 106, India

ARTICLE INFO

Keywords:
Square duct
Wall shear stress
Direct numerical simulation
OpenFOAM

ABSTRACT

Direct numerical simulations (DNS) of turbulent flow through a square duct at two different low Reynolds numbers is performed using OpenFOAM to study the instantaneous wall shear stress fluctuations and near-wall structures. We first benchmarked our simulation results against other DNS studies which used higher-order spectral methods, thereby confirming the accuracy of our results. The mean profile of streamwise wall shear stress is well studied in the literature, however its higher order statistics has not been yet explored. There is also a lack of information on the spanwise component of wall shear stress and its higher-order statistics. Here, we provide an extensive study on streamwise and spanwise wall shear stresses, and their higher-order statistics. The intensities of both components of wall shear stress fluctuations are close to zero near the corner, and monotonically increase while moving towards the duct center. This is in contrast with their mean profiles which do not exhibit similar monotonic trends. However, the third-order moment, i.e. skewness of the streamwise wall shear stress again shows a non-monotonic behavior from the corner to the center. The profiles of the mean as well as the higher-order statistics of wall shear stress follow a better scaling between the two Reynolds number studied, when the spanwise location is normalized using inner scaling. Streamwise velocity correlations near the wall show that the flow structures in a square duct are similar to that of a channel flow near the center, whereas there is a cross-talk of the flow structures between the neighboring walls near the corner. An investigation into the effect of corner on the probability of back flow events is made at a Reynolds number lower than previously reported. The probability follows a non-monotonic behavior as we move from the corner towards the center, where it reaches a minimum at around 50 wall units from the corner. Similar to the wall shear stress profiles, the behavior of the near-wall flow structures as well as the spanwise variation of the probability of backflow events also show a qualitatively similar trend for the two Reynolds numbers, when the spanwise location is normalized using inner scaling.

1. Introduction

The presence of corners in a square duct gives rise to non-zero cross-stream components of the mean velocity, which are known as 'Prandtl's secondary flow of the second kind' [1]. These secondary flows, although being only a few percentage of the mean velocity in magnitude, may have a significant impact on the primary flow properties such as skin friction [2]. After pioneering works by Nikuradse [3], various experimental works have been conducted to better understand this phenomenon [2,4,5]. Gessner [2] investigated the origin of secondary flow in a turbulent square duct and found that the secondary flow is mainly a consequence of the Reynolds shear stress gradient in the corner region. The first direct numerical simulation (DNS) of flow through a square duct was conducted by Gavrilakis [6]. The flow was simulated for a friction Reynolds number of $Re_\tau = 150$ ($Re_\tau = \overline{u_\tau} h/\nu$, where $\overline{u_\tau}$ is the friction velocity averaged over the duct perimeter, h is the duct half-height and ν is the kinematic viscosity, note some authors define Re_τ based on the full duct height i.e. $2h$). This condition corresponded to the bulk Reynolds number of $Re_b = 2205$, where $Re_b = U_b h/\nu$ and U_b is the bulk (or average) velocity. It was observed that the corners make the time-averaged streamwise wall shear stress to be non-uniformly distributed around the duct. Huser and Biringen [7] carried out a DNS for square duct flow at $Re_b = 5160$. They investigated the mechanism for the existence of secondary flow using quadrant analysis and by examining instantaneous flow structures. Zhang et al.

* Corresponding author at: Fluid and Complex Systems Research Centre, Coventry University, Coventry, CV1 5FB, UK.
E-mail address: ragrawal@liverpool.ac.uk (R. Agrawal).

https://doi.org/10.1016/j.compfluid.2022.105688
Received 11 November 2021; Received in revised form 11 September 2022; Accepted 4 October 2022
Available online 13 October 2022

Table 1
Summary of some of the major numerical works conducted to study turbulent flow through a square duct. h is the half-height of the duct.

Authors	Simulation type	Re_b	Re_τ	Dimensions of domain
Madabhushi and Vanka [13]	LES	2905	180	$2h \times 2h \times 4\pi h$
Gavrilakis [6]	DNS	2205	150	$2h \times 2h \times 20\pi h$
Pattison et al. [17]	GLBE and LES	–	150	$2h \times 2h \times 12h$
Pinelli et al. [10]	DNS	1077–3500	80–225	$2h \times 2h \times (10.97 - 12.57)h$
Zhang et al. [8]	DNS	2206–10 714	150–600	$2h \times 2h \times 4\pi h$
Pirozzoli et al. [9]	DNS	2205–20 000	150–1055	$2h \times 2h \times 6\pi h$
Present	DNS	1596, 3000	109.7, 194.5	$2h \times 2h \times 6\pi h$

[8] carried out DNS for square duct flow for Reynolds numbers in the range $Re_b = 2206 - 10\,714$. They observed a significant low-Reynolds number effect for $Re_b = 2206$. Pirozzoli et al. [9] further investigated the square duct flow using DNS for a wide Reynolds number range, $Re_b = 2205 - 20\,000$. They observed a weak dependence of intensity of secondary motions on the range of Reynolds numbers studied. Pinelli et al. [10] studied square duct flow at various (low) Reynolds numbers $Re_b = 1077$ to $Re_b = 3500$. These Reynolds numbers range from a so-called "marginal" state to fully turbulent flow. They tried to explain the mechanism for the presence of local extrema (minima and maxima) of the mean streamwise wall shear stress along the width of the duct. This distribution was found to be due to the preferential location of the low- and high-speed streaks, where these streaks have a typical average spacing of $\Delta S^+ \approx 50$, where $\Delta S^+ = \Delta S\overline{u_\tau}/\nu$ [11]. They observed that with increasing Reynolds number the variation in the mean streamwise wall shear stress across the duct gradually smoothes out, except near the corner where the high-speed streaks remain visible. Other than DNS, large eddy simulations (LES) has also been used to study square duct flow. LES filters the small-scale information of the turbulent flow and therefore reduces the cost of simulation [12]. Madabhushi and Vanka [13] used LES to investigate square duct flow at $Re_b = 2905$ and Xu and Pollard [14] used LES to investigate the annular square duct flow (flow between two square ducts where the inner duct is solid) at $Re_b = 3349$ (based on half the hydraulic diameter of the annular duct). Vázquez and Métais [15] and [16] studied the flow through a square duct with heat transfer using LES. Pattison et al. [17] used a generalized lattice Boltzmann equation (GLBE) in conjunction with LES to study a square duct flow. For fully turbulent flows, the square duct is generally characterized by the presence of eight counter-rotating vortices normal to the streamwise direction, first observed by Nikuradse [3]. Uhlmann et al. [18] carried out DNS for so-called marginally turbulent flow and observed two different flow states at $Re_b = 1077$, where each state contained only four vortex instead of the conventional eight vortex. Later, Owolabi et al. [19] also observed similar behavior in experiments. The Reynolds numbers studied in the present case are large enough to be outside of this "marginally-turbulent" state. Table 1 shows some of the major numerical investigations carried out using DNS and LES to study the square duct flows. It also shows the Reynolds numbers studied and the size of the computational domain used for the simulation.

For wall-bounded flows, instantaneous wall shear fluctuations have been found to contain information about the flow above the wall [20]. In this regard, the two most well-studied canonical wall-bounded flows are channel flow and boundary layer flow. Extensive investigations into the fluctuating wall shear stress have been made for these two flows [21–25]. Until now, the study of the wall shear stress in square duct flow has been limited to the mean characteristics of the streamwise wall shear stress. The spanwise component of wall shear stress has been studied for the case of channel flow (for example, see [21,22]). However, to the best of the authors' knowledge, the characteristics of instantaneous spanwise wall shear stress for a square duct flow has not been previously reported. Near-wall velocity correlations are also well investigated for channel and boundary layer flows [26,27]. The streamwise velocity correlations are generally marked by the presence of a positive correlation flanked by two negative correlations on either side. The effect of corners on the near-wall velocity correlations has not been studied and forms an additional motivation for the present study.

A type of extreme or rare event previously observed in channel flow are so-called "backflow events" [22,24,28]. These events are generally found near the wall and are characterized by the instantaneous streamwise velocity being less than zero i.e. negative indicating flow reversal or "back" flow. Hu et al. [22], using DNS for channel flow at $Re_b = 2818$, obtained the probability of occurrence of these back-flow events to be about 1.35×10^{-4}. Lenaers et al. [28] observed a potential connection between the modulation of the near-wall region by the large-scale motions in the outer region and the backflow events. Brücker [29] carried out an experimental investigation of backflow events in a zero pressure gradient (ZPG) boundary layer flow using micro-pillar sensors. It was found that the backflow events are correlated with strong gradients of spanwise component of wall shear stress. Cardesa et al. [30] performed an extensive investigation into the structure and dynamics of these backflow events for channel flow using DNS. Chin et al. [31] investigated the backflow events in the presence of Prandtl's secondary flow of the first kind (i.e. driven by pipe curvature) by comparing the flow through a toroidal pipe and a straight pipe. Recently, Zaripov et al. [32,33] investigated the reverse flow formation mechanism in square duct flow at $Re_b \simeq 3100$ using DNS as well as experiments. They suggested that the higher probability of these backflow events near the corner in a square duct is related to the presence of streamwise oriented vortical structures and is driven by a different mechanism to those observed closer to the duct center and in channel flow. However, the existence and probability of these backflow events at lower Reynolds numbers in the presence of corners have not been reported. Investigating backflow events at lower Reynolds numbers is particularly challenging using DNS, as the probability of occurrence of these events decreases with decreasing Re_b [22]. Therefore, a longer computational time is needed to detect these "very-rare" events at low Re_b. In this work, we compare our results for $Re_b = 3000$ with the Zaripov et al. [32] and show a good agreement with them, and also show new results for $Re_b = 1596$.

In recent years, an open source computational fluid dynamics software OpenFOAM, which is based on the finite-volume method, has been widely used to study turbulent flow. Although this software uses lower order schemes for the discretization which potentially reduces the accuracy of the results compared to the higher order spectral methods (such as *Channelflow,* [34]), many studies have shown that good agreement with higher order methods can be achieved with suitable care. Komen et al. [35] studied pipe and channel flow using second order accurate OpenFOAM for different mesh sizes with and without a SGS (sub-grid scale) LES model. They showed that using sufficient grid resolution an accurate mean and fluctuation intensities of the velocity fields can be obtained. OpenFOAM has been shown to work well for DNS study of different kinds of flows, for example electromagnetically forced flows [36], turbulent reacting flows [37], compressible reacting flows [38], and drag-reducing flows [39]. The LES of square duct flows has been carried out in the past using OpenFOAM by Schindler et al. [16], however, based on our knowledge, no corresponding DNS study is available in the literature. Therefore, one of the aims of the current study is to examine the efficacy of OpenFOAM to study the DNS of square duct flows, which is a relatively complex flow compared to channel and pipe flows due to the presence of mean secondary flows.

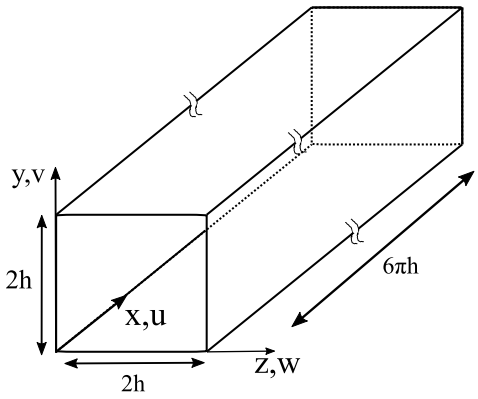

Fig. 1. Computational domain and coordinate system.

We have also chosen OpenFOAM as the computational tool in order to ultimately study the effects of polymer addition in square duct flows in a future study.

In this paper, we explore both streamwise and spanwise components of instantaneous wall shear stress extensively for $Re_b = 1596$ and 3000. Thus the primary motivations of the paper are three-fold: to investigate the role of the side wall on the mean statistics of the wall shear stress, on the near-wall flow structure, and on the rare backflow events. Another motivation of this work is to investigate the accuracy of OpenFOAM in simulating turbulent square duct flow. The rest of the paper is organized as follows: the governing equations and numerical procedure employed here is discussed in Section 2. Section 3 presents the extensive validation of the numerical method. Section 4 discusses the first and second-order wall shear stress statistics. Section 5 shows the higher-order statistics of the wall shear stress. Near-wall streamwise velocity correlations are presented and discussed in Section 6. Section 7 discusses the rare near-wall backflow events. Finally, the conclusions of the present work are presented in Section 8.

2. Numerical methodology

We consider an incompressible flow in a duct of square cross-section. A Cartesian coordinate system is employed with x, y and z being the coordinates, with x being the streamwise direction and y, z being the cross-stream directions. The computational domain and the coordinate system employed is shown in Fig. 1. The non-dimensional form of the Navier–Stokes equations are employed, given by:

$$\nabla \cdot \mathbf{u} = 0, \tag{1}$$

$$\frac{\partial \mathbf{u}}{\partial t} + \mathbf{u} \cdot \nabla \mathbf{u} = -\nabla p + \frac{1}{Re_b} \nabla^2 \mathbf{u}. \tag{2}$$

Here, Reynolds number is given by $Re_b = hU_b/\nu$. No-slip and no-penetration boundary conditions are used at the wall and a periodic boundary condition is applied in the streamwise direction.

The present study utilizes a finite-volume method based on the open source CFD software OpenFOAM [40]. A second-order accurate backward differencing scheme is used for the time integration. For spatial discretization, second-order accurate linear schemes are used for both convective and diffusive fluxes. A summary of the various discretization schemes used in this study are provided in Table 2. PISO (Pressure-Implicit with Splitting of Operators) algorithm, developed by Issa [41] and Issa et al. [42], is applied for the pressure–velocity coupling. The details of this algorithm can be found in [43].

Two different Reynolds numbers are investigated, $Re_b = 1596$ and 3000. For $Re_b = 1596$, $N_y \times N_z \times N_x = 156 \times 156 \times 400$ cells are used. However, two different meshes are considered to examine the effect of mesh resolution for $Re_b = 3000$, by considering a base mesh which has $N_y \times N_z \times N_x = 192 \times 192 \times 480$ cells and a fine mesh which has $N_y \times N_z \times N_x = 256 \times 256 \times 600$ cells. These two meshes are considered to specifically study the dependency of the statistics on the mesh sizes, given a second-order accuracy of the present method. A uniform mesh is used for the x direction for both Reynolds numbers, whereas an algebraic stretching of the mesh has been used for the cross-flow (y and z) directions with a cell expansion ratio of 10. This means the ratio of the width of the cell at the center is 10 times the first cell close to the wall. This provides the first grid location from the wall at $y^+ = 0.17$ for $Re_b = 1596$, and at $y^+ = 0.25$ for the base mesh and $y^+ = 0.19$ for the fine mesh for $Re_b = 3000$. At the duct center, the width of the cell is $\Delta y^+ = 3.1$ for $Re_b = 1596$, and $\Delta y^+ = 5.03$ for the base mesh and $\Delta y^+ = 3.84$ for the fine mesh for $Re_b = 3000$. The time-step is kept such that the Courant–Friedrichs–Lewy (CFL) number is less than 0.6. The initial condition for the mean velocity field is the laminar profile superimposed with a random noise. We ensure that the flow has reached a fully-developed state before starting the statistical analysis. Statistics are then accumulated over a period of $TU_b/h = 10\,800$ for $Re_b = 1596$ and $TU_b/h = 4300$ for $Re_b = 3000$. A convergence test, using the higher-order statistics of the wall shear stress, has been carried out. It is observed that the statistics are well-converged for the data accumulation time. A summary of details of the numerical simulations is provided in Table 3. The Re_τ values, shown in the second row of Table 3, are calculated using the area- and time-averaged wall shear stress data.

Table 2
Discretization schemes.

ddtSchemes	Backward	Second order
gradSchemes	Gauss linear	Second order
divSchemes	Gauss linear	Second order
LaplacianSchemes	Gauss linear orthogonal	Second order
interpolationSchemes	Linear	Second order
snGradSchemes	Orthogonal	Second order

Table 3
Flow parameters for the DNS of square duct flow. T and N_f are the time interval and the number of flow fields used for averaging, respectively.

Re_b	1596	3000	3000
Re_τ (calc.)	109.7	194.4	194.5
L_x	$6\pi h$	$6\pi h$	$6\pi h$
$N_y \times N_z \times N_x$	156 × 156 × 400	192 × 192 × 480	256 × 256 × 600
$\Delta y_w^+, \Delta z_w^+$	0.17	0.25	0.19
$\Delta y_c^+, \Delta z_c^+$	3.1	5.03	3.84
Δx^+	5.14	7.54	6.14
TU_b/h	10 800	4300	4300
N_f	10 800	4300	4300

In the past, researchers have used different streamwise lengths of the square duct for the simulations. For example, Pinelli et al. [10] used $L_x \simeq 4\pi h$, Vinuesa et al. [44] used $L_x = 8\pi h$, Zhang et al. [8] used $L_x = 4\pi h$ and Pirozzoli et al. [9] used $L_x = 6\pi h$. We have utilized a computational domain with a streamwise extent of $L_x = 6\pi h$. Two-point velocity correlations were calculated to determine that the duct is sufficiently long to avoid any numerical artefacts due to periodic boundary conditions for the streamwise direction. The correlation coefficient is given by:

$$R_{kk} = \frac{\overline{k(x)k(x+\Delta x)}}{\sigma(k)^2}. \tag{3}$$

Here, k can be streamwise velocity fluctuations (u'), wall-normal velocity fluctuations (v') or spanwise velocity fluctuations (w'). $u' = U - \langle U \rangle(z)$, $v' = V - \langle V \rangle(z)$ and $w' = W - \langle W \rangle(z)$, where $\langle U \rangle(z)$, $\langle V \rangle(z)$ and $\langle W \rangle(z)$ are the time- and streamwise-averaged streamwise, wall-normal and spanwise velocities, respectively. $\sigma(k)$ is the root mean square (RMS) of k. The correlations are calculated for the lower left quadrant of the duct, i.e. $0 < y^* < 0.5$ and $0 < z^* < 0.5$. Here, superscript

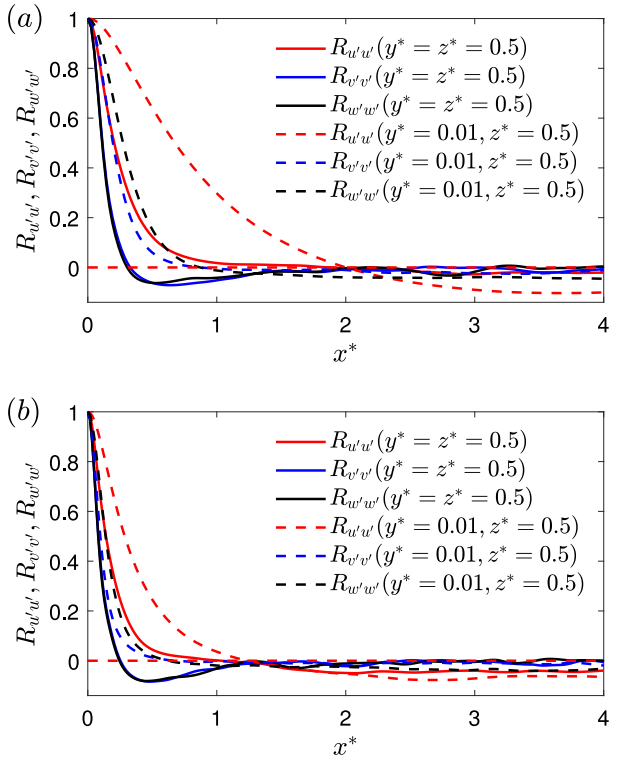

Fig. 2. Two-point velocity correlation coefficients for (a) Re_b = 1596 and (b) Re_b = 3000.

$*$ denotes scaling using $2h$, i.e. $z^* = z/2h$. In Fig. 2, the correlation coefficients are shown for all three velocity components at two spatial locations $y^* = z^* = 0.5$, and $y^* = 0.01$, $z^* = 0.5$. It can be seen that all the velocity components decorrelate by $x^* \approx 2$ for $Re_b = 1596$ and by about $x^* \approx 1.2$ for $Re_b = 3000$. We have chosen a computational domain of length $x^* = 3\pi$. This is much longer than $x^* = 2$ as given by the velocity correlations. A longer domain is chosen in order to be able to study the rare large-scale structures present in the near-wall region of the wall-bounded flow [45,46]. However, this study does not form a part of this current paper.

3. Validation of simulation results

Fig. 3 shows a comparison of the friction factor value with previous studies and Jones' correlation [47], which is given by:

$$1/f^{1/2} = 2\log(2.25Re_b f^{1/2}) - 0.8. \tag{4}$$

Here, $f = 8\overline{u_\tau}^2/U_b^2$. The results are shown for both fine and base mesh cases for $Re_b = 3000$. A good agreement can be observed between Jones' correlation and the present results for both $Re_b = 1596$ and 3000.

Fig. 4(a) shows the mean streamwise velocity and the mean secondary flow vectors. As expected, the time-averaged secondary flow vectors reveal the presence of two counter-rotating streamwise vortices near the corner of the square duct. These secondary motions are known for transferring the momentum from the duct core to its corner [7]. Fig. 4(b) shows the mean streamwise vorticity, which is given by:

$$\langle\omega_x\rangle = \frac{\partial\langle V\rangle}{\partial z} - \frac{\partial\langle W\rangle}{\partial y}. \tag{5}$$

To calculate the mean velocity profiles, an octant averaging (across the four walls) as well as time and streamwise averaging of the profiles have been carried out. Similar averaging for the profiles of the wall shear stress statistics has been carried out in the rest of this paper.

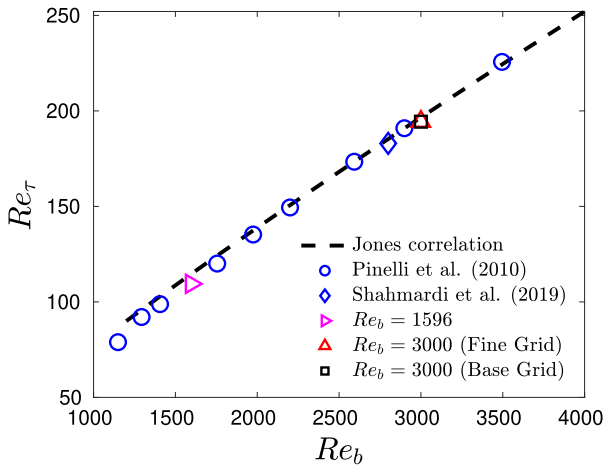

Fig. 3. Variation of Re_τ with Re_b.

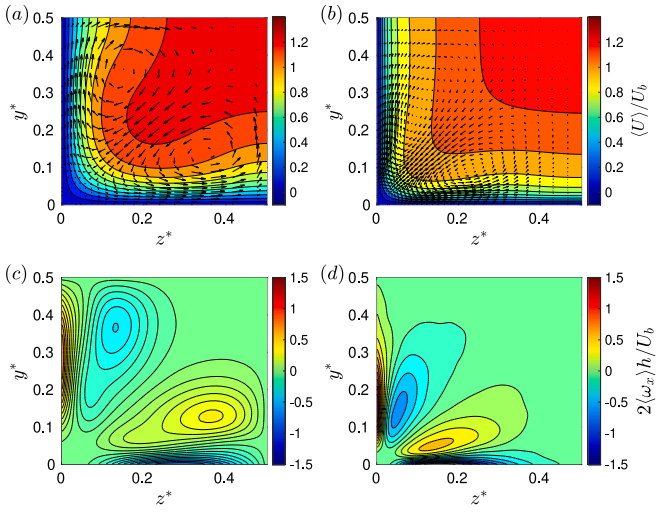

Fig. 4. Iso-contours of mean streamwise velocity for the first quadrant for (a) Re_b = 1596 and (b) Re_b = 3000. The streamwise velocity is normalized by U_b. The mean secondary flow vectors are shown as black arrows (every fourth vector is shown). Contours of mean streamwise vorticity averaged over the four quadrants for (c) Re_b = 1596 and (d) Re_b = 3000. Here, the vorticity is normalized by $U_b/2h$. Results are shown for fine mesh case for Re_b = 3000.

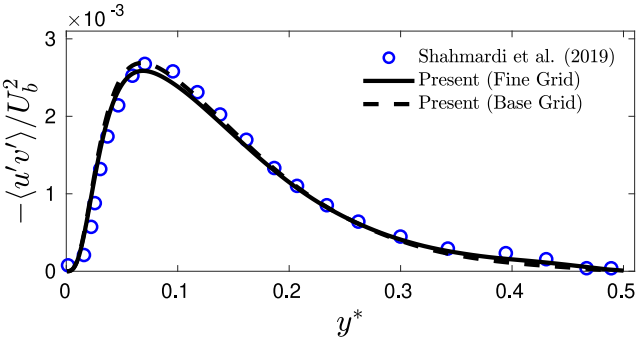

Fig. 5. Mean $u'v'$ component of the Reynolds stress tensor profile in bulk units at z^* = 0.2 for Re_b = 3000. Circles represent the result by Shahmardi et al. [48] at Re_b = 2800.

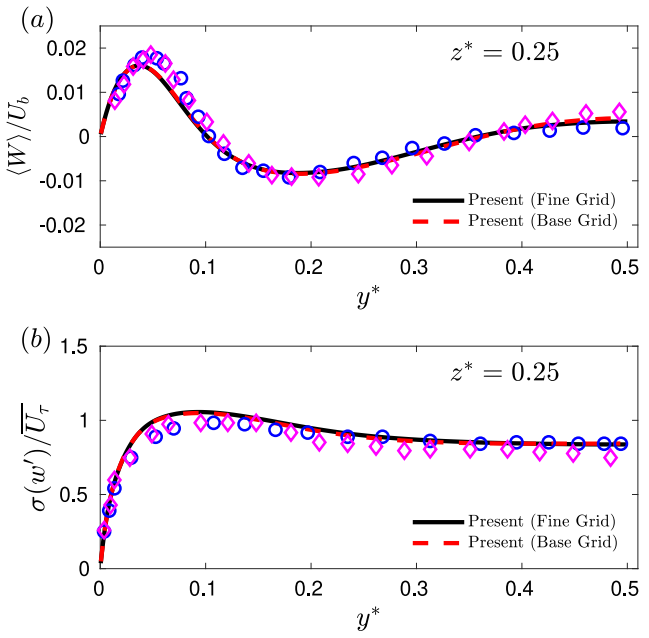

Fig. 6. Profiles of (a) mean spanwise velocity and (b) spanwise velocity fluctuation as a function of the wall-normal distance at $z^* = 0.25$ for $Re_b = 3000$. Purple diamonds indicate results by Gavrilakis [6] at $Re_b = 2205$ and blue circles indicate results by Vázquez and Métais [15] at $Re_b = 3000$.

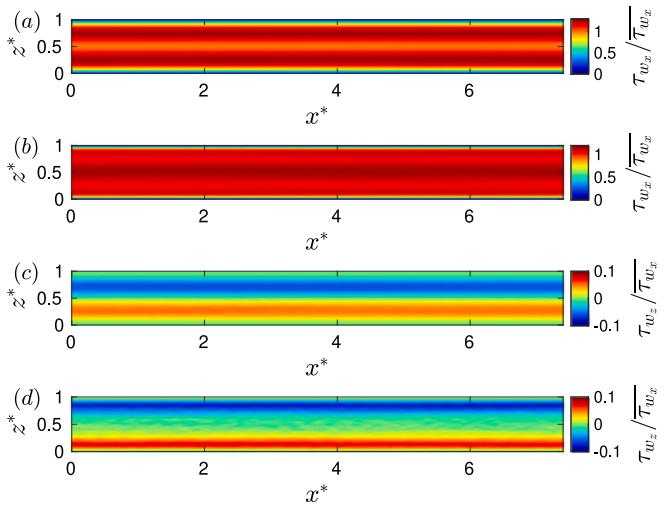

Fig. 7. Spatial patterns of the section of ensemble-averaged streamwise wall shear stress at (a) $Re_b = 1596$ and (b) $Re_b = 3000$. Spatial patterns of ensemble-averaged spanwise wall shear stress at (c) $Re_b = 1596$ and (d) $Re_b = 3000$. Here, the wall shear stress values are normalized by the time- and area-averaged streamwise wall shear stress, $\overline{\tau_{w_x}}$.

In this section, the purpose of studying the profiles is to investigate the robustness of our numerical procedure by comparing the profiles present in the literature. Therefore, the velocities are scaled in the same manner as done by these original authors for the corresponding profile. Fig. 5 compares the uv component of the Reynolds shear stress tensor at $z^* = 0.2$ for $Re_b = 3000$ with [48]. A good agreement between results can be observed. Fig. 6 shows the mean spanwise velocity and spanwise velocity fluctuations at a spanwise distance of $z^* = 0.25$ for $Re_b = 3000$. The present result is compared with [6] at $Re_b = 2205$ and Vázquez and Métais [15] at $Re_b = 3000$. A good agreement between the previous works and our results can also be observed. Taken together, these comparisons with other benchmark studies confirm the robustness and accuracy of our numerical approach using OpenFOAM. In the rest of the sections, results are only shown for the fine mesh data, however no significant differences were found between the base and fine mesh cases.

4. First- and second-order statistics

Wall shear stress has two components: streamwise wall shear stress (τ_{w_x}) and spanwise wall shear stress (τ_{w_z}), where $\tau_{w_x} = \mu(\partial U/\partial x)_w$ and $\tau_{w_z} = \mu(\partial W/\partial z)_w$ [21]. A first-order differencing is employed to calculate the gradient using the first cell from the wall, which is well within the viscous sublayer ($y^+ < 1$). This is a reasonable approximation because of the linear velocity profile in the viscous sublayer region [49]. There are significant differences in the wall shear stress fields between the channel flow and square duct flow. Unlike DNS of channel flow (which assumes a periodic boundary condition in the spanwise direction), the mean streamwise wall shear stress is not uniform in the spanwise direction of the square duct due to the presence of corners. The time-averaged spanwise wall shear stress is not necessarily zero everywhere on the duct wall, unlike the channel flow employing spanwise periodic boundary conditions [21,22]. The shape of the mean streamwise wall shear stress profile in a square duct flow is related to the number of high- and low-speed streaks present at the wall. Fig. 7 shows the spatial patterns of ensemble-averaged streamwise and spanwise wall shear stresses, where x and z are normalized in outer units. Here, averaging over the four walls and different flow fields has been conducted to carry out the ensemble-averaging. The results here are shown only for x^* up to around 7.4, however the total length of x^* is 3π. Fig. 7a and b show the ensemble-averaged streamwise wall shear stress for $Re_b = 1596$ and $Re_b = 3000$, respectively. The contours for these two Reynolds numbers are qualitatively different from each other. For $Re_b = 1596$, there exists a low τ_{w_x} region near the center, followed by high τ_{w_x} regions on either side of the center, and then the τ_{w_x} decreases until it reaches to zero at the corner. Whereas, for $Re_b = 3000$, there is a region of high τ_{w_x} near the center, followed by low τ_{w_x} regions on both sides and then again the high τ_{w_x} region and finally, it goes to zero near the corner. Results for $Re_b = 3000$ is qualitatively similar to that obtained by Shahmardi et al. [48] at $Re_b = 2800$ for the Newtonian case, where they observed the presence of two minima and three maxima in the streamwise wall shear stress profile, where the two maxima were located close to the corner and one at the center. Each minimum was located between the two maxima. The ensemble-averaged spanwise wall shear stress is shown in Fig. 7c and d for $Re_b = 1596$ and $Re_b = 3000$, respectively. There is an opposite sign of the mean values on each side of the wall. This is because of the change in the direction of the spanwise wall shear stress relative to the center. However, the spanwise-averaged τ_{w_z} should necessarily be zero, as there is no mean force acting in the spanwise direction. In contrast to τ_{w_x}, the τ_{w_z} shows a qualitatively similar picture for both Reynolds numbers i.e. its value increases from zero at the duct corner, reaches a maximum and then gets down to zero again at the duct mid-wall. However, the locations of this maxima is different for the two Reynolds numbers, when outer scaling is used for normalizing z. This behavior is further investigated by comparing the effects of outer and inner scalings on the wall shear stress profiles in the next paragraph.

Fig. 8(a) shows the mean wall shear stresses ($\langle \tau_{w_x} \rangle, \langle |\tau_{w_z}| \rangle$) normalized using $\overline{\tau_{w_x}}$. The data for both base and fine meshes are shown for $Re_b = 3000$ and a good agreement can be seen between the two profiles for both $\langle \tau_{w_x} \rangle$ and $\langle \tau_{w_z} \rangle$. Similar to Fig. 7, for $Re_b = 1596$, the $\langle \tau_{w_x} \rangle$ starts from zero at the corner and reaches a local maximum and then a local minimum at the duct centerline, as we move along the z direction. For $Re_b = 3000$, the $\langle \tau_{w_x} \rangle$ starts from zero at the corner and reaches a local maximum, a local minimum and finally another local maximum at the duct centerline, as we move along the z direction. The average spanwise wall shear stress increases from zero to a maximum

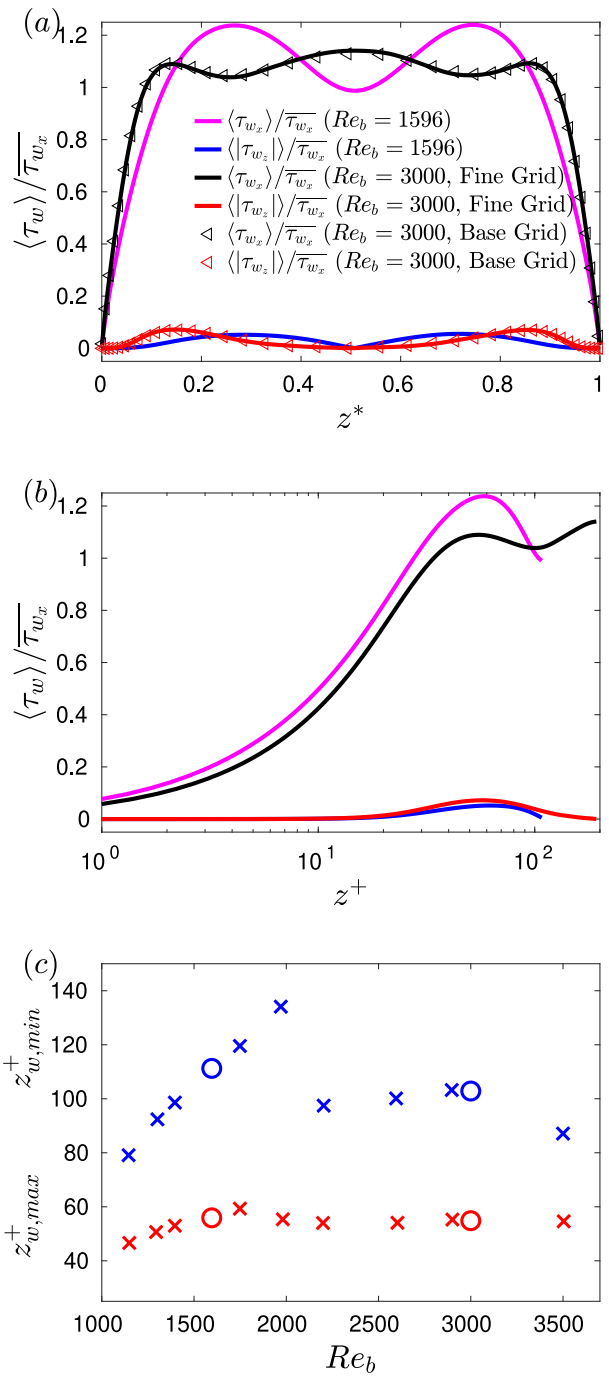

Fig. 8. Wall shear stress along the wall of the duct normalized by the area-averaged streamwise wall shear stress, $\overline{\tau_{w_x}}$, where x-axis is shown in (a) outer units and (b) inner units. (c) Distance of the maximum (red symbols) and minimum (blue symbols) values of the mean streamwise wall shear stress in wall units. Cross represents the result obtained by Pinelli et al. [10] and circle represents the result obtained in the present study.

value and decreases back to zero near the mid-wall location for both the Reynolds numbers. The maximum value of $\langle\tau_{w_z}\rangle/\overline{\tau_{w_x}}$ is less than 10 times than the maximum $\langle\tau_{w_x}\rangle/\overline{\tau_{w_x}}$ for both Reynolds numbers. The locations for the maxima and minima seems to not scale well between the two Reynolds numbers when the spanwise locations are normalized using outer units ($z^* = z/2h$). Therefore, we examine these mean values (and also the other statistical quantities in the later sections) while normalizing the spanwise locations in wall or inner units ($z^+ = zu_\tau/\nu$).

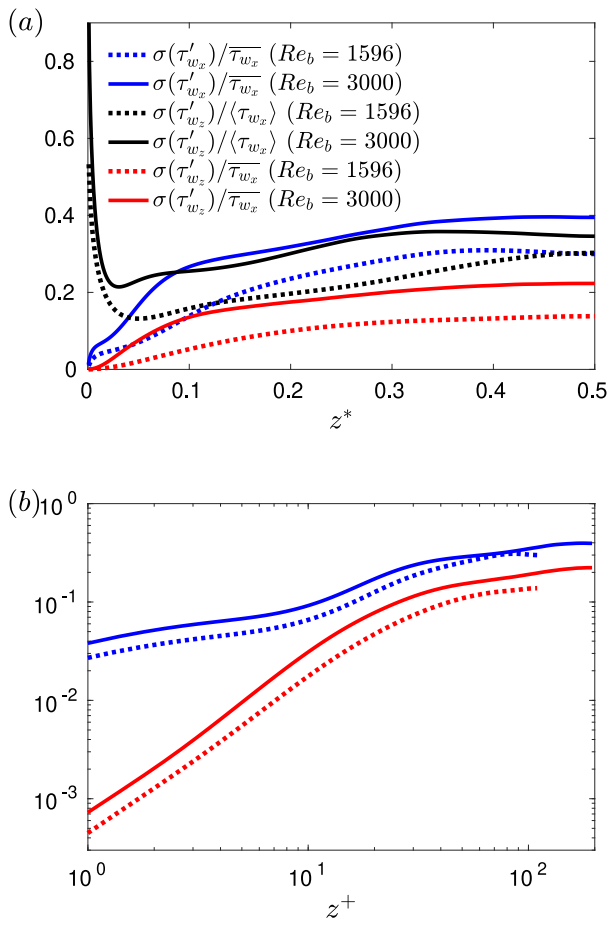

Fig. 9. Variation of normalized RMS of streamwise and spanwise wall shear stresses with the spanwise location, where x-axis is shown in (a) outer unit and (b) inner unit. The lines in (b) represent the same data as in (a).

Fig. 8(b) shows the same data as 8(a), however the x-axis is replaced with z^+. Now, we can see that the local maxima for the $\langle\tau_{w_x}\rangle$ occurs at about $z^+ \approx 50$ for both Reynolds numbers. Interestingly, $\langle\tau_{w_z}\rangle$ also seem to scale well with varying z^+ for the two Reynolds numbers. The $\langle\tau_{w_z}\rangle$ remains almost zero up to about $z^+ \approx 10$ and starts to increase with the maxima of $\langle\tau_{w_z}\rangle$ for both Reynolds numbers occurring at about $z^+ \approx 60$. After $z^+ \approx 60$, they start to decrease again and finally decays to zero at the centerline.

Fig. 8(c) shows the distances of the maxima and minima of $\langle\tau_{w_x}\rangle/\overline{\tau_{w_x}}$ closest from the corner. The distances are shown in inner or wall units i.e. $z^+_{w,max} = z_{w,max}u_\tau/\nu$ and $z^+_{w,min} = z_{w,min}u_\tau/\nu$, where $z_{w,max}$ and $z_{w,min}$ are the distances of the maximum and minimum values of the mean streamwise wall shear stress closest from the corner, respectively. The present results are compared with the data obtained by Pinelli et al. [10] for square duct flows, and a good agreement is observed between these two results. This agreement also further validates the accuracy of our simulation results. The $z^+_{w,max}$ for both Re_b occurs at $z^+ \approx 55$. The $z^+_{w,min}$ for $Re_b = 1596$ is at $z^+ \approx 110$, which is basically the centerline of the duct. However, the $z^+_{w,min}$ for $Re_b = 3000$ is at $z^+ \approx 103$. As explained by Pinelli et al. [10], for $Re_b \approx 1077$ - 2000, the low speed streak is preferentially located at the centerline, flanked by two high speed streaks. At $Re_b \approx 2000$, there is a sharp change in the position of the minimum, indicating that five streaks are now present along the wall.

Streamwise and spanwise wall shear stress fluctuations are calculated by subtracting the instantaneous values with the corresponding time- and streamwise-averaged values: $\tau'_{w_x}(z) = \tau_{w_x}(z) - \langle\tau_{w_x}\rangle(z)$ and

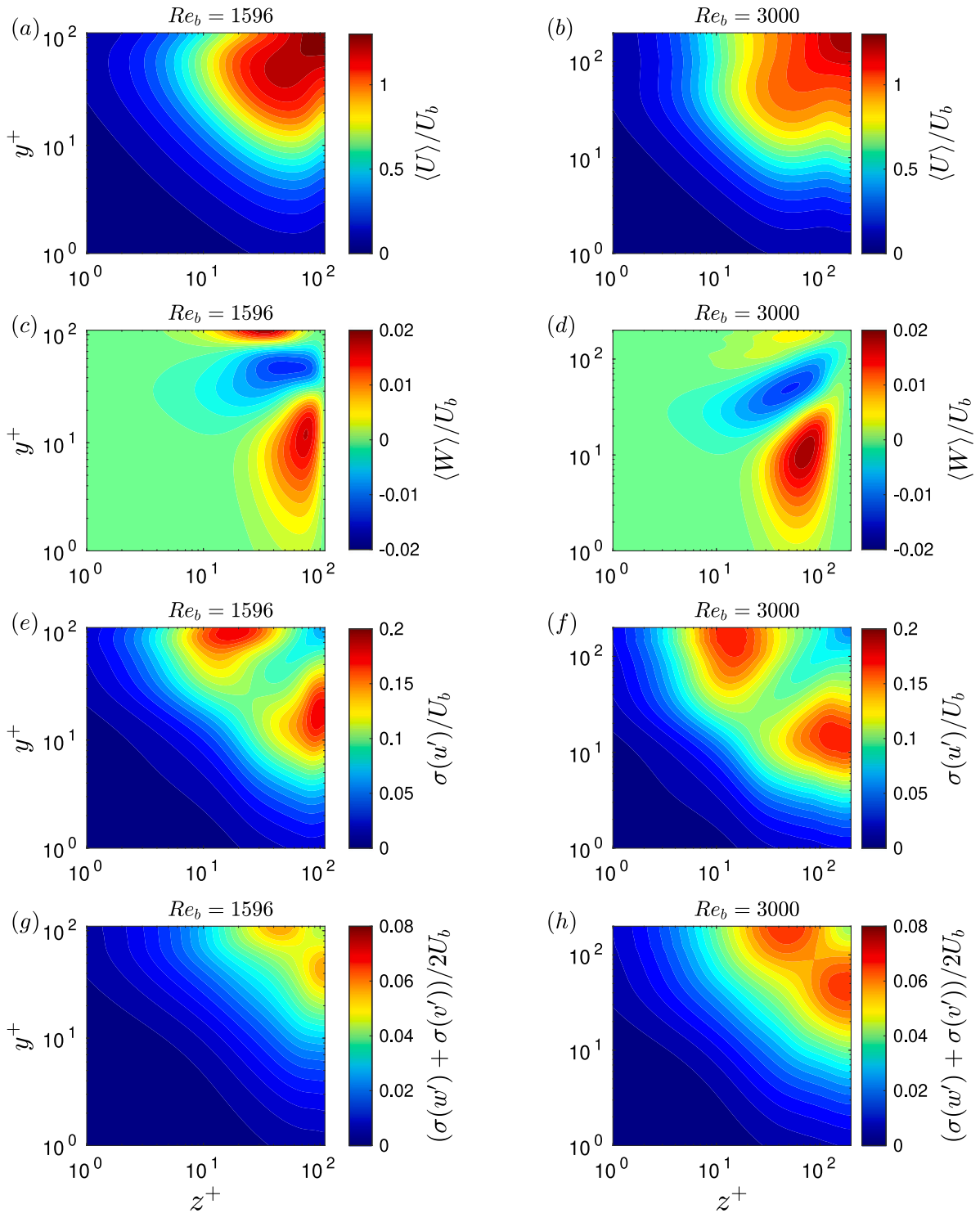

Fig. 10. Contours of time-averaged (a, b) streamwise velocity, (c, d) spanwise velocity, (e, f) streamwise velocity fluctuations intensity and (g, h) average of wall-normal and spanwise velocity fluctuations intensity, where (a, c, e, g) are the results for $Re_b = 1596$ and (b, d, f, h) are the results for $Re_b = 3000$. All the mean and fluctuation quantities are normalized using the bulk velocity.

$\tau'_{w_z}(z) = \tau_{w_z}(z) - \langle \tau_{w_z} \rangle(z)$. Second-order statistics (i.e. RMS, σ) is then calculated using these fluctuations. Fig. 9 shows the normalized RMS of streamwise and spanwise wall shear stress fluctuations. Both outer and inner scalings are utilized for normalizing the spanwise locations, and are shown in Fig. 9(a) and (b), respectively. When normalized with the time-, streamwise- and area-averaged streamwise wall shear stress ($\overline{\tau_{w_x}}$), the RMS of both streamwise and spanwise wall shear stress fluctuations are very low near the corner of the square duct, indicating a very low level of turbulence. This normalized RMS increases monotonically as we move towards the center of the duct. However, when normalized with the $\langle \tau_{w_x} \rangle$ (which does not includes area-averaging), the RMS shows a higher value near the corner of the duct. This is expected as the mean value of the streamwise wall shear stress is very low near the corner, as also shown in Fig. 8. This high value of the

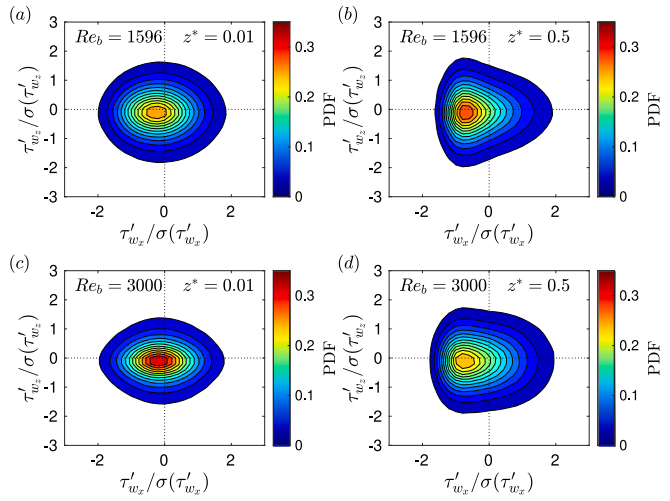

Fig. 11. Joint distributions of normalized streamwise and spanwise wall shear stress fluctuations for spanwise locations of (a, (c) $z^* = 0.01$ and (b, (d) $z^* = 0.5$. (a, b) and (c, d) are the results for $Re_b = 1596$ and $Re_b = 3000$, respectively.

normalized RMS then rapidly decreases to a minimum, and after this location, it increases and reaches an approximately asymptotic value. Compared to Fig. 9(a), (b) shows a better scaling of the RMS values between the two Reynolds numbers when the spanwise location is normalized in inner units. The normalized streamwise and spanwise wall shear stress RMS values ($\sigma(\tau'_{w_x})/\overline{\tau_{w_x}}$ and $\sigma(\tau'_{w_z})/\overline{\tau_{w_x}}$) follow similar trends for the two Reynolds numbers, with the respective values being higher for $Re_b = 3000$ at all spanwise locations. The $\sigma(\tau'_{w_z})/\overline{\tau_{w_x}}$ remains comparable yet consistently lower than the $\sigma(\tau'_{w_x})/\overline{\tau_{w_x}}$ for all the spanwise locations for both Reynolds numbers. A lower value of the $\sigma(\tau'_{w_z})/\overline{\tau_{w_x}}$ compared to the $\sigma(\tau'_{w_x})/\overline{\tau_{w_x}}$ has also been previously observed for channel flow [22]. There is a change in the slope for $\sigma(\tau'_{w_x})/\overline{\tau_{w_x}}$ and $\sigma(\tau'_{w_z})/\overline{\tau_{w_x}}$ at about $z^+ \approx 20$. After this z^+ location, the increase in the RMS values slow down and approximately reaches an asymptotic value. $\langle\tau_{w_x}\rangle/\overline{\tau_{w_x}}$ profile, as shown in Fig. 8, depends on the number of low and high speed streaks present at the wall, whereas, the corner suppresses its intensity ($\sigma(\tau'_{w_x})/\overline{\tau_{w_x}}$) profile up to close to the center. $\sigma(\tau'_{w_z})/\overline{\tau_{w_x}}$ also shows a monotonic increase from corner to center, unlike its mean which exhibits a peak at $z^+ \approx 60$. To probe the intensities further, we look into the contours of the first two moments of the velocities in the duct.

Fig. 10 shows the time- and streamwise-averaged contours of the first two moments of the two (streamwise and spanwise) velocity components in the wall-normal (y) - spanwise (z) plane. Here, in Fig. 10(g, h), an average of the intensities of wall-normal and spanwise velocity components is shown, as this is an unambiguous way of showing the cross-stream intensity as it does not depend on which side of the wall is our reference. The results are shown only for the first quadrant ($0 < y^* < 0.5$ and $0 < z^* < 0.5$) of the duct. The wall-normal and spanwise locations are normalized in wall units. As stated before, there is a linear correlation between the wall shear stress and velocity gradient in the viscous sub-layer ($y^+, z^+ \leq 5$), and therefore the velocity values in this region directly represent the wall shear stress values. Closer to the wall (i.e. for $y^+, z^+ \leq 5$), the contour lines of the $\langle U\rangle/U_b$ and $\langle W\rangle/U_b$ are non-monotonic while moving from the duct corner to the center. This behavior is also shown in Fig. 8, while discussing the mean wall shear stress profiles. However, the $\sigma(u')/U_b$ and $(\sigma(w') + \sigma(v'))/2U_b$ values are increasing monotonically close to the wall as we move from the corner to the center. This remains consistent with the behavior of the $\sigma(\tau'_{w_x})/\overline{\tau_{w_x}}$ and $\sigma(\tau'_{w_z})/\overline{\tau_{w_x}}$ profiles as shown in Fig. 9. This is also in contrast with their variation along the wall-normal axis at the center where their values are non-monotonic as we move from the bottom wall to the duct center.

5. Probability density functions and third-order statistics

Fig. 11 shows the joint probability distribution functions (jPDFs) of the normalized streamwise and spanwise wall shear stress fluctuations near the corner ($z^* = 0.01$) and at the center ($z^* = 0.5$). The spanwise wall shear stress fluctuations remain approximately symmetric for both locations at either Reynolds number. The streamwise wall shear stress fluctuations are nearly symmetric at $z^* = 0.01$. Closer to the duct center, however, the streamwise wall shear stress fluctuations become positively skewed. Positive skewness of streamwise wall shear stress fluctuations is well-known for the case of turbulent channel flows [22,50]. The joint distributions look qualitatively different for the two Reynolds numbers at the center, where for $Re_b = 1596$, the distribution is "arrow-shaped" along the x-axis whereas for $Re_b = 3000$, the distribution is more elliptical. This behavior is further investigated using the PDF plots.

We look into the PDF of streamwise and spanwise wall shear stress fluctuations in Fig. 12(a, b, c) and (d), respectively. Here, the PDFs are shown on a logarithmic scale in order to direct attention to their tails. The tails of the PDFs are also known to be related to the presence of rare events in a turbulent flow [49]. As shown in Fig. 12(a, b), for the streamwise wall shear stress, the "left" (i.e. negative) side of the tail monotonically shifts towards zero while moving from the corner to the centerline for both Reynolds numbers. However, the right (positive) side of the tail does not exhibit such monotonic behavior. For $Re_b = 3000$, the PDFs at $z^*(z^+) = 0.14$ (54), 0.28 (109) and 0.5 (194.5) are very close to each other, where these three locations correspond to the local extrema of the mean streamwise wall shear stress. This suggests that although the intensities of the fluctuations at these locations are different (as shown in Fig. 9), when the fluctuations are normalized by their RMS values the structure at these locations share similar PDFs, i.e. the distribution is basically self-similar. However, for $Re_b = 1596$, the PDFs at the two extrema of the mean streamwise wall shear stress i.e. at $z^*(z^+) = 0.28$ (61) and 0.5 (109.7) are not similar, suggesting a potential low Reynolds number effect. To further study the difference between the jPDFs at $z^* = 0.5$ for the two Reynolds numbers as shown in 11, we compare the PDFs of streamwise wall shear stress fluctuations in Fig. 12(c). It can be seen that the two PDFs do not quite collapse on each other. This is not surprising, as it has been shown in channel flow that the PDFs or the higher order statistics of streamwise wall shear stress changes with Reynolds numbers, especially for low Reynolds number flow [22]. For the spanwise wall shear stress, the PDFs (as shown in Fig. 12d) at $z^* = 0.5$ collapse on each other for the two Reynolds numbers, and the difference between the tails remain indiscernible. Although the PDF tails for the spanwise wall shear stress are largely symmetric, they are still far from being Gaussian indicating that large fluctuations do still occur fairly frequently.

The third order moment, also called the skewness, of the wall shear stress fluctuations is given by $S(\tau'_w) = \overline{\tau'^3_w}/\sigma(\tau'_w)^3$. As shown in Fig. 13, $S(\tau'_{w_z})$ remains close to zero for all the spanwise locations. This reinforces the conclusion obtained from Fig. 11 (where the joint pdfs were almost symmetric about the horizontal axis) that spanwise wall shear stress fluctuations has approximately the same probability to be either positive or negative. However, the $S(\tau'_{w_x})$ shows a non-monotonic behavior as a function of the spanwise location for both Reynolds numbers. For $Re_b = 1596$, the $S(\tau'_{w_x}) \approx 0.18$ near the duct corner and it increases as we move towards the center for up to $z^*(z^+) \approx 0.1(22)$. After this spanwise location, there is a dip in the $S(\tau'_{w_x})$, where the local minima occurs at about $z^*(z^+) \approx 0.18(39)$, then the skewness increases until the duct center. For $Re_b = 3000$, $S(\tau'_{w_x})$ is close to zero near the duct corner and it increases as we move towards the center for up to $z^*(z^+) \approx 0.05(20)$. After this spanwise location, there is a slight dip in the $S(\tau'_{w_x})$, where the local minima occurs at about $z^*(z^+) \approx 0.12(49)$ and there is an another local maximum at about $z^*(z^+) \approx 0.27(107)$. Following this spanwise location, the skewness decreases and reaches an asymptotic value of about 0.97 at the duct

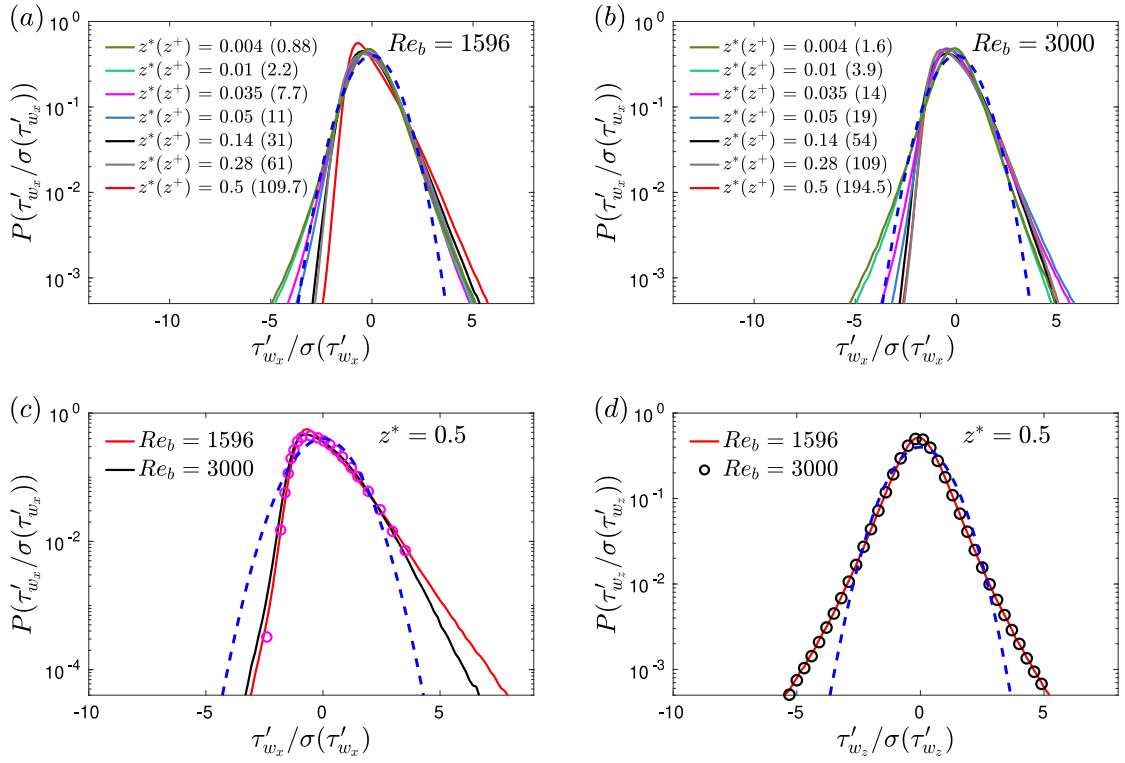

Fig. 12. (a, b) PDFs of normalized streamwise wall shear stress fluctuations for $Re_b = 1596$ and $Re_b = 3000$, respectively. (c) PDFs of normalized streamwise wall shear stress fluctuations at $z^* = 0.5$ for $Re_b = 1596$ and $Re_b = 3000$, respectively. Purple open circles show the data obtained by Hu et al. [22] for channel flow at $Re_b = 2818$. (d) PDFs of normalized spanwise wall shear stress fluctuations for $Re_b = 1596$ and $Re_b = 3000$ at $z^* = 0.5$, respectively. Blue dashed lines show a Gaussian PDF in all the figures.

center. We can see a better scaling of the $S(\tau'_{w_x})$ data between the two Reynolds numbers when the spanwise locations are normalized using inner units. One stark difference in $S(\tau'_{w_x})$ between these two Reynolds numbers is their non-uniform difference as we move from the corner to the duct center, where the value for $Re_b = 1596$ is higher in the corner region as well as near the center. The skewness of the wall shear stress fluctuations is further probed using contours of the skewness of streamwise velocity fluctuations, as shown in Fig. 14. The $S(u')$ near the wall (up to $y^+ \approx 8-10$) is higher at $z^+ \approx 20$ for both Reynolds numbers. After this z^+ location, the $S(u')$ value decreases and then increases again and reaches a maximum at about $z^+ \approx 105$, which is close to the center for $Re_b = 1596$. However, for $Re_b = 3000$, the $S(u')$ decreases after $z^+ \approx 105$ and reaches approximately a constant value up to the center. This explains the reason for higher $S(\tau'_{w_x})$ near the center for $Re_b = 1596$ compared to $Re_b = 3000$.

6. Near-wall streamwise velocity correlations

To investigate the near-wall structures, two-point spatial correlations of streamwise velocity are calculated. The correlation is calculated using Eq. (6), where the subscript '0' denotes the center of correlation. For $Re_b = 1596$, the correlations are calculated for two spanwise locations z_0^* (z_0^+) = 0.28 (61) and 0.5 (109.7). For $Re_b = 3000$, the correlations are calculated for three spanwise locations z_0^* (z_0^+) = 0.14 (54), 0.28 (109) and 0.5 (194.5). These locations correspond to the local extrema of the mean streamwise wall shear stress as shown in Fig. 8(a).

$$R_{uu}(\Delta x, \Delta y, \Delta z) = \frac{\overline{u'(x_0+\Delta x, y_0+\Delta y, z_0+\Delta z)u'(x_0, y_0, z_0)}}{\sigma(u'(x_0, y_0, z_0))^2}. \quad (6)$$

The wall-normal location is fixed at $y_0^* = 0.008$ for both Reynolds numbers, giving $y_0^+ = 1.75$ for $Re_b = 1596$ and $y_0^+ = 3.11$ for $Re_b = 3000$. These locations lie in the so-called viscous sub-layer and therefore, the streamwise velocity at this wall-normal location can be used to represent the streamwise wall shear stress. Two different streamwise locations $x_0^* = 2$ and $x_0^* = 7$ are utilized to calculate the correlations in order to provide better statistical results. These two streamwise locations are not correlated with each other, as shown in Fig. 2. The correlations are calculated only for the lower wall and no quadrant averaging has been carried out to make sure there is no smearing of the results due to cross-talk between the walls. We visualize the correlations using isosurface representation. Using isosurfaces for visualizing the correlations is slightly subjective as we need to provide an appropriate threshold. Fig. 15 shows 3-D views as well as 2-D slices of the correlations for $Re_b = 1596$ in the wall-normal - spanwise plane. Here, the red isosurface corresponds to $R_{uu,iso} = 1.2$ and the blue isosurface corresponds to $R_{uu,iso} = -0.8$. Near the mid-wall region (z_0^* (z_0^+) = 0.5 (109.7)), the correlations are symmetric i.e. a region of positive correlation flanked by negative correlations on both sides. This is qualitatively similar to distributions observed earlier for channel and boundary-layer flows [26,27]. However, for z_0^* (z_0^+) = 0.28 (61), the correlation is no longer symmetric for the same side of the duct wall. The positive correlation is still flanked by two negative correlations, however one of the negative correlations shifts onto the neighboring duct wall. This suggests the presence of a cross-talk between the neighboring walls of the duct close to the corner. Fig. 16 shows 3-D views as well as 2-D slices of the correlations $Re_b = 3000$ in the wall-normal - spanwise plane. Here, the red isosurface corresponds to $R_{uu,iso} = 0.3$ and the blue isosurface corresponds to $R_{uu,iso} = -0.3$. A qualitatively similar correlation to channel flow can be observed for z_0^* (z_0^+) = 0.5 (194.5) and 0.28 (109). However, for z_0^* (z_0^+) = 0.14 (54), the correlation is similar to as observed for $Re_b = 1596$ at z_0^* (z_0^+) = 0.28 (60), i.e. a positive correlation is flanked by two negative correlations where one of them is on the neighboring wall. Therefore, the correlations obtained at these two Reynolds numbers show a qualitatively similar trend for the same z^+ and not same z^*.

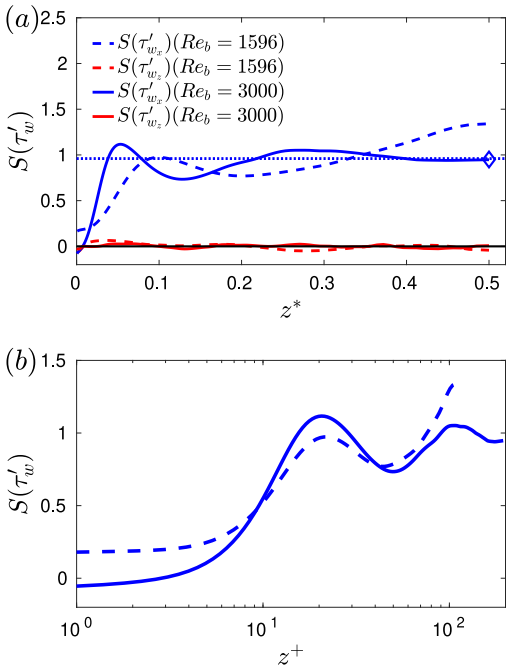

Fig. 13. Variation of skewness of streamwise and spanwise wall shear stress fluctuations with the spanwise location, where x-axis is shown in (a) outer unit and (b) inner unit. The lines in (b) represent the same data as in (a). Blue dotted line in (a) represents the skewness of streamwise wall shear stress fluctuations for channel flow obtained by Hu et al. [22] using DNS for $Re_b = 2818$. Blue diamond in (a) highlights the skewness of streamwise velocity obtained by Gavrilakis [6] for $Re_b = 2205$ at $z^* = 0.5$ and $y^* = 0.00075$.

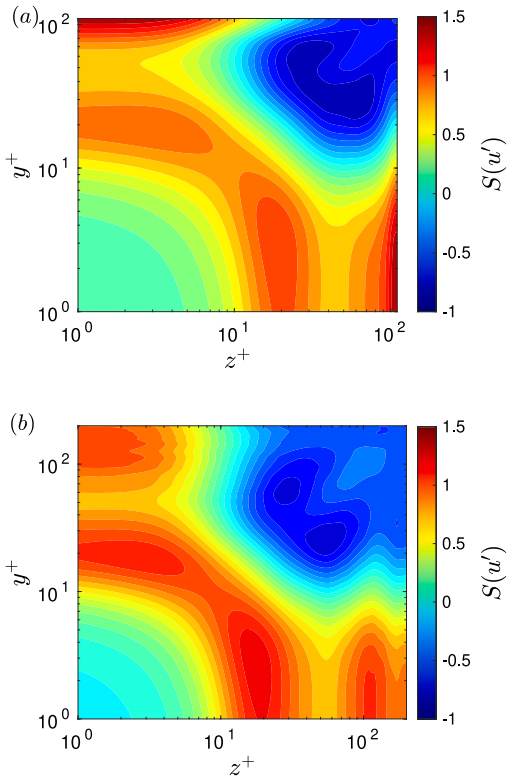

Fig. 14. Contours of time-averaged skewness of streamwise velocity fluctuations for (a) $Re_b = 1596$ and (b) $Re_b = 3000$.

7. Near-wall backflow events

We examine the so-called backflow events in the near-wall region of a square duct using the instantaneous streamwise wall shear stress information. Fig. 17 shows the percentage (P_{bf}) of occurrence of negative wall shear stress events as a function of the spanwise location. The results shown in Fig. 17 are time- and octant-averaged. Two interesting phenomena can be observed; firstly the presence of a higher value of percentage of negative wall shear stress events very close to the corner, and secondly, a non-monotonic behavior of this fraction as we move towards the center. Near the centerline for $Re_b = 3000$, the percentage reaches close to the corresponding values for channel flow as obtained by Hu et al. [22]. The present results are also compared with the recent result by Zaripov et al. [32] at $Re_b = 3150$ for square duct flow. The paper of Zaripov et al. [32] discusses the physical mechanism behind the increased probability for backflow events in the vicinity of the sidewall. Based on Fig. 17, it can be said that there is a strong effect of the corner on the probability of occurrence of back flow events. The P_{bf} scales well between the two Reynolds numbers for varying z^+, as shown in 17. The P_{bf} values are lower for $Re_b = 1596$ by almost an order of magnitude compared to $Re_b = 3000$ at all z^+. This is consistent with the previously observed results for channel flow where the frequency of backflow events were found to increase with Reynolds numbers [22]. The minimum value of P_{bf} occurs at about $z^+ \approx 50$ for both the Reynolds numbers.

Next, we examine the PDFs of streamwise wall shear stress normalized by the time- and area-averaged value, shown in Fig. 18. The negative streamwise wall shear stress events or the backflow events have a much higher probability for the flow very close to the corner for both the Reynolds numbers. As we move closer to the centerline, the left hand side of the tails start to approach zero and approximately collapse on one another. However, a non-monotonic trend of the right hand side tails while getting closer to the zero value can be observed. A slightly different tail, showing a relatively lower probability of back flow events, can be seen at $z^+ = 54$ for $Re_b = 3000$. This is consistent with the lower P_{bf} values at this z^+ location as shown in Fig. 17.

8. Conclusions

A DNS study of turbulent flow in a square duct was carried out for $Re_b = 1596$ and 3000 using OpenFOAM. A good agreement of the mean statistics with the past works is observed which validates OpenFOAM as an effective tool to study turbulent square duct flows. The corners have a significant influence on the statistics of the wall shear stress and the near-wall structures. Both outer and inner scaling are used to normalize the spanwise locations in order examine their relevance on various wall shear stress statistics and near-wall structures. The intensities of the wall shear stress fluctuations are very low near the corner and increases monotonically moving towards the center. This is in contrast to the mean wall shear stress which shows a non-monotonic behavior moving from corner to the center. The skewness of the streamwise wall shear stress fluctuations is non-monotonic moving from the corner to the center. However, the skewness of spanwise wall shear stress fluctuations remain close to zero at all spanwise locations for both Reynolds numbers. The profiles of the mean as well as the higher-order wall shear stress statistics show qualitatively similar trends with varying z^+ for $Re_b = 1596$ and 3000. To further investigate the wall shear stress statistics, we probed the velocity statistics above the wall. The near-wall structures are studied using the near-wall velocity correlations. A change in the characteristics of the velocity correlations is observed while moving the center of correlation from the corner towards the center. At about $z^+ \approx 50 - 60$ for both Reynolds numbers, the positive correlation is flanked by two negative correlations, where each one of them is on the neighboring walls. At about $z^+ \geq 100$, the positive correlation is flanked by two negative correlations on the same wall, a behavior typically observed in channel and boundary layer flows.

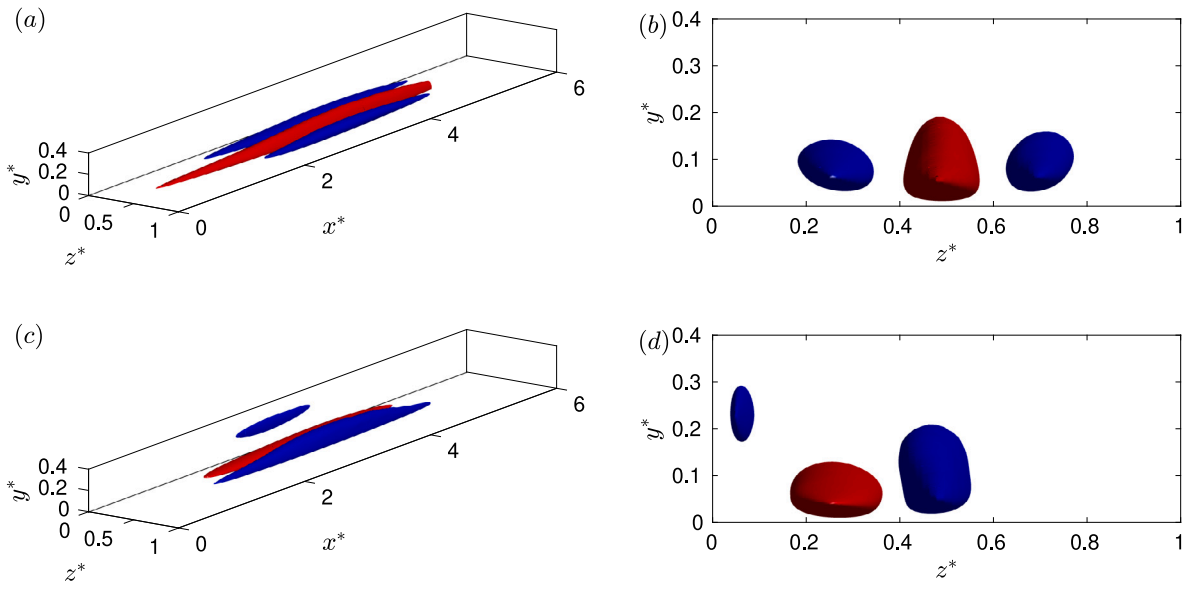

Fig. 15. Time-averaged correlation of streamwise velocity fluctuations for $Re_b = 1596$. The correlations are calculated for streamwise center of correlations of $x_0^* = 2$ and 7, and then averaged. The wall-normal center of correlation is $y_0^* = 0.008$ ($y_0^+ = 1.75$). The spanwise center of correlations are: (a, (b) $z_0^* = 0.5$, (c, (d) $z_0^* = 0.28$. Blue iso-surface: $R_{uu,iso} = -0.8$ and red iso-surface: $R_{uu,iso} = 1.2$ for every case shown.

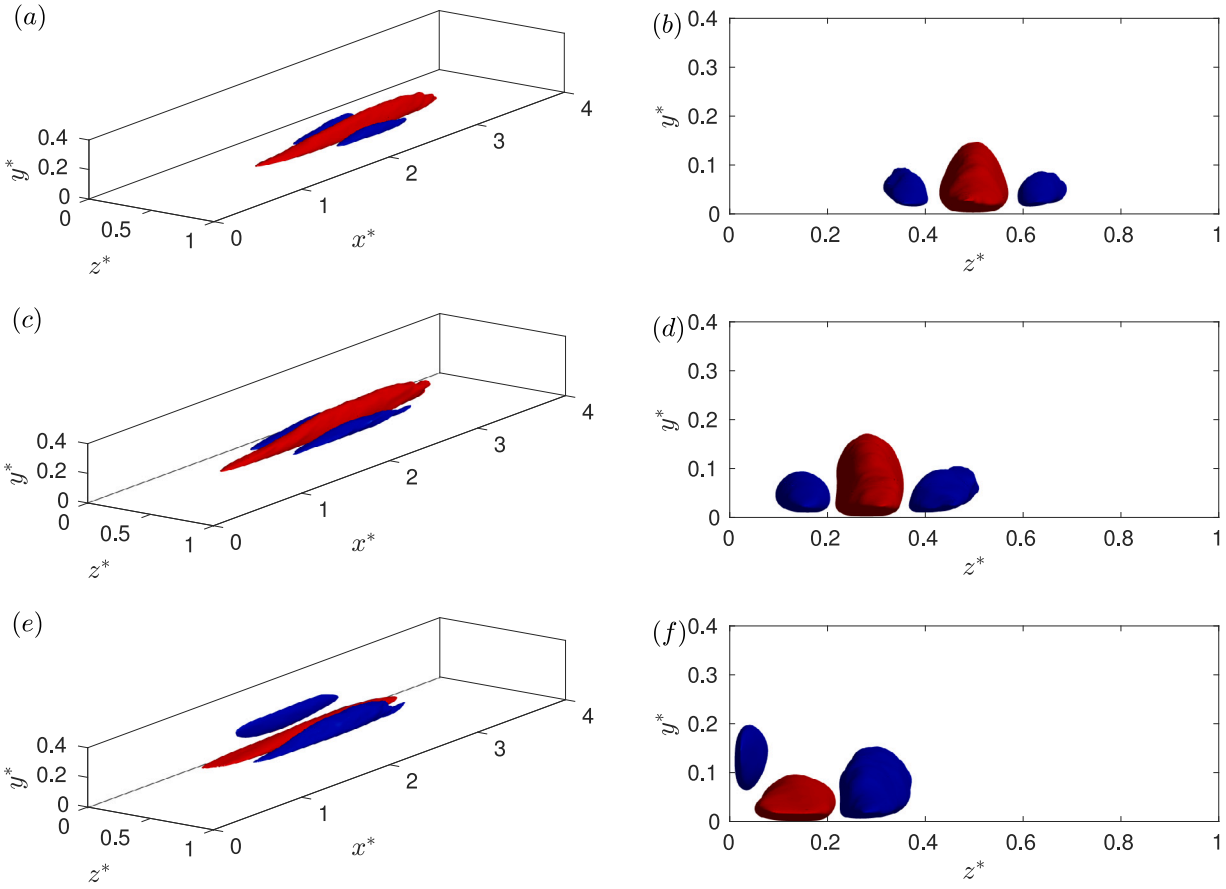

Fig. 16. Time-averaged correlation of streamwise velocity fluctuations for $Re_b = 3000$. The correlations are calculated for streamwise center of correlations of $x_0^* = 2$ and 7, and then averaged. The wall-normal center of correlation is $y_0^* = 0.008$ ($y_0^+ = 3.11$). The spanwise center of correlations are: (a, (b) $z_0^* = 0.5$, (c, (d) $z_0^* = 0.28$, (e, (f) $z_0^* = 0.14$. Blue iso-surface: $R_{uu,iso} = -0.3$ and red iso-surface: $R_{uu,iso} = 0.3$ for every case shown.

This shows a presence of cross-talk of the flow structures between the neighboring walls closer to the corner. The probability of backflow events follow a non-monotonic trend as we move from the duct corner to the center, where it is highest near the corner and goes to a minima at about $z^+ \approx 50$, then increases, and finally reaches an approximately constant value near the center. The probability of backflow events for

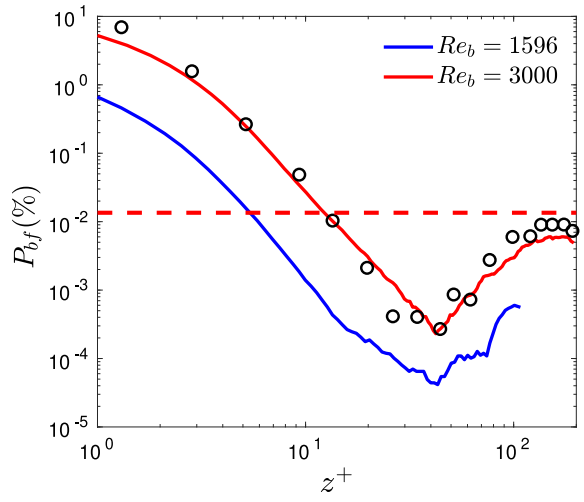

Fig. 17. Percentage (P_{bf}) of negative streamwise wall shear stress as a function of the spanwise distance. Black open circles show the result obtained by Zaripov et al. [32] for Re_b = 3150 in a square duct flow. Red dashed line represents the result obtained by Hu et al. [22] for channel flow at $Re_b = 2818$.

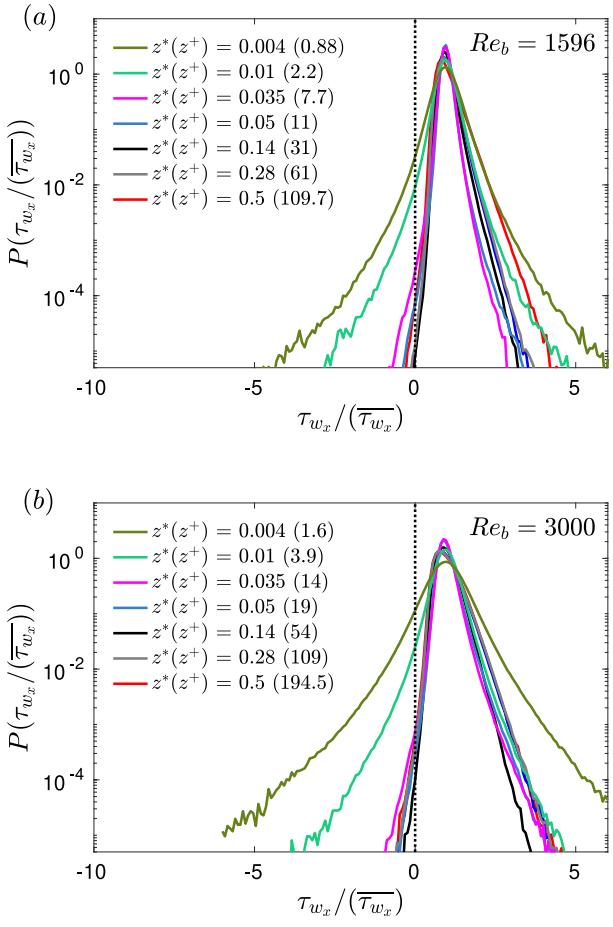

Fig. 18. PDF of normalized streamwise wall shear stress for various spanwise locations for (a) Re_b = 1596 and (b) Re_b = 3000.

Re_b = 1596 remains almost an order of magnitude lower than for Re_b = 3000. Similar to the flow statistics, the near-wall structures as well as the probability of the near-wall backflow show a similar trend for both the studied Reynolds numbers with varying z^+.

Overall, it can be seen that when inner scaling is used for normalization, the wall shear stress shows similar characteristics between the two Reynolds numbers. However, low-Reynolds number effects can be observed for Re_b = 1596 while comparing the third-order statistics and the PDFs of wall shear stress at the center. This result is consistent with effects scaling on inner (wall) units such that as Reynolds number is increased, side wall effects are confined "closer" (i.e in outer units) to the side walls and the side walls have less overall affect on the dynamics.

CRediT authorship contribution statement

Rishav Agrawal: Conceptualization, Methodology, Software, Validation, Formal analysis, Investigation, Writing – original draft. **Debi Prasad Mishra:** Conceptualization, Supervision, Writing – review & editing. **Robert J. Poole:** Supervision, Methodology, Project administration, Writing – review & editing.

Declaration of competing interest

The authors declare that they have no known competing financial interests or personal relationships that could have appeared to influence the work reported in this paper.

Data availability

Data will be made available on request.

Acknowledgment

R. A. is thankful to the HPC facility provided by Coventry University where all the numerical simulations have been carried out.

References

[1] Prandtl L. Uber die ausgebildete turbulenz. verh 2nd intl kong fur tech mech, zurich. Engl Transl: NACA Tech Memo 1926;62:435.
[2] Gessner F. The origin of secondary flow in turbulent flow along a corner. J Fluid Mech 1973;58(1):1–25.
[3] Nikuradse J. Untersuchungen über turbulente Strömungen in nicht kreisförmigen rohren. Ing-Arch 1930;1(3):306–32.
[4] Gessner F, Jones J. On some aspects of fully-developed turbulent flow in rectangular channels. J Fluid Mech 1965;23(4):689–713.
[5] Melling A, Whitelaw J. Turbulent flow in a rectangular duct. J Fluid Mech 1976;78(part 2):289–315.
[6] Gavrilakis S. Numerical simulation of low-Reynolds-number turbulent flow through a straight square duct. J Fluid Mech 1992;244:101–29.
[7] Huser A, Biringen S. Direct numerical simulation of turbulent flow in a square duct. J Fluid Mech 1993;257:65–95.
[8] Zhang H, Trias FX, Gorobets A, Tan Y, Oliva A. Direct numerical simulation of a fully developed turbulent square duct flow up to Reτ=1200. Int J Heat Fluid Flow 2015;54:258–67.
[9] Pirozzoli S, Modesti D, Orlandi P, Grasso F. Turbulence and secondary motions in square duct flow. J Fluid Mech 2018;840:631–55. http://dx.doi.org/10.1017/jfm.2018.66.
[10] Pinelli A, Uhlmann M, Sekimoto A, Kawahara G. Reynolds number dependence of mean flow structure in square duct turbulence. J Fluid Mech 2010;644:107–22.
[11] Kim J, Moin P, Moser R. Turbulence statistics in fully developed channel flow at low Reynolds number. J Fluid Mech 1987;177:133–66.
[12] Sagaut P. Large eddy simulation for incompressible flows: an introduction. Springer Science & Business Media; 2006.
[13] Madabhushi RK, Vanka SP. Large eddy simulation of turbulence-driven secondary flow in a square duct. Phys Fluids A 1991;3(11):2734–45.
[14] Xu H, Pollard A. Large eddy simulation of turbulent flow in a square annular duct. Phys Fluids 2001;13(11):3321–37.
[15] Vázquez MS, Métais O. Large-eddy simulation of the turbulent flow through a heated square duct. J Fluid Mech 2002;453:201.

[16] Schindler A, Younis B, Weigand B. Large-eddy simulations of turbulent flow through a heated square duct. Int J Therm Sci 2019;135:302–18.
[17] Pattison MJ, Premnath KN, Banerjee S. Computation of turbulent flow and secondary motions in a square duct using a forced generalized lattice Boltzmann equation. Phys Rev E 2009;79(2):026704.
[18] Uhlmann M, Pinelli A, Kawahara G, Sekimoto A. Marginally turbulent flow in a square duct. J Fluid Mech 2007;588:153–62.
[19] Owolabi BE, Poole RJ, Dennis DJ. Experiments on low-Reynolds-number turbulent flow through a square duct. J Fluid Mech 2016;798:398–410.
[20] Marusic I, Mathis R, Hutchins N. Predictive model for wall-bounded turbulent flow. Science 2010;329(5988):193–6.
[21] Jeon S, Choi H, Yoo JY, Moin P. Space–time characteristics of the wall shear-stress fluctuations in a low-Reynolds-number channel flow. Phys Fluids 1999;11(10):3084–94.
[22] Hu ZW, Morfey CL, Sandham ND. Wall pressure and shear stress spectra from direct simulations of channel flow. AIAA J 2006;44(7):1541–9.
[23] Örlü R, Schlatter P. On the fluctuating wall-shear stress in zero pressure-gradient turbulent boundary layer flows. Phys Fluids 2011;23(2):021704.
[24] Diaz-Daniel C, Laizet S, Vassilicos JC. Wall shear stress fluctuations: Mixed scaling and their effects on velocity fluctuations in a turbulent boundary layer. Phys Fluids 2017;29(5):055102.
[25] Agrawal R, Ng HC-H, Dennis DJ, Poole RJ. Investigating channel flow using wall shear stress signals at transitional Reynolds numbers. Int J Heat Fluid Flow 2020;82:108525.
[26] Monty J, Stewart J, Williams R, Chong M. Large-scale features in turbulent pipe and channel flows. J Fluid Mech 2007;589:147.
[27] Dennis DJ, Nickels TB. Experimental measurement of large-scale three-dimensional structures in a turbulent boundary layer. Part 1. Vortex packets. J Fluid Mech 2011;673:180.
[28] Lenaers P, Li Q, Brethouwer G, Schlatter P, Örlü R. Rare backflow and extreme wall-normal velocity fluctuations in near-wall turbulence. Phys Fluids 2012;24(3):035110.
[29] Brücker C. Evidence of rare backflow and skin-friction critical points in near-wall turbulence using micropillar imaging. Phys Fluids 2015;27(3):031705.
[30] Cardesa J, Monty J, Soria J, Chong M. The structure and dynamics of backflow in turbulent channels. J Fluid Mech 2019;880.
[31] Chin R, Vinuesa R, Örlü R, Cardesa J, Noorani A, Chong M, Schlatter P. Backflow events under the effect of secondary flow of Prandtl's first kind. Phys Rev Fluids 2020;5(7):074606.
[32] Zaripov D, Ivashchenko V, Mullyadzhanov R, Li R, Markovich D, Kähler CJ. Reverse flow phenomenon in duct corners at a low Reynolds number. Phys Fluids 2021;33(8):085130.
[33] Zaripov D, Ivashchenko V, Mullyadzhanov R, Li R, Mikheev N, Kähler CJ. On a mechanism of near-wall reverse flow formation in a turbulent duct flow. J Fluid Mech 2021;923.
[34] Gibson JF. Channelflow: A spectral Navier-Stokes simulator in C++. Technical report, U. New Hampshire; 2014, Channelflow.org.
[35] Komen E, Camilo L, Shams A, Geurts BJ, Koren B. A quantification method for numerical dissipation in quasi-DNS and under-resolved DNS, and effects of numerical dissipation in quasi-DNS and under-resolved DNS of turbulent channel flows. J Comput Phys 2017;345:565–95.
[36] Habchi C, Antar G. Direct numerical simulation of electromagnetically forced flows using OpenFOAM. Comput & Fluids 2015;116:1–9.
[37] Vo S, Kronenburg A, Stein OT, Hawkes ER. Direct numerical simulation of non-premixed syngas combustion using OpenFOAM. In: High performance computing in science and engineering´ 16. Springer; 2016, p. 245–57.
[38] Li T, Pan J, Kong F, Xu B, Wang X. A quasi-direct numerical simulation solver for compressible reacting flows. Comput & Fluids 2020;213:104718.
[39] Zheng E, Rudman M, Singh J, Kuang S. Direct numerical simulation of turbulent non-Newtonian flow using openfoam. Appl Math Model 2019;72:50–67.
[40] Weller HG, Tabor G, Jasak H, Fureby C. A tensorial approach to computational continuum mechanics using object-oriented techniques. Comput Phys 1998;12(6):620–31.
[41] Issa RI. Solution of the implicitly discretised fluid flow equations by operator-splitting. J Comput Phys 1986;62(1):40–65.
[42] Issa RI, Gosman A, Watkins A. The computation of compressible and incompressible recirculating flows by a non-iterative implicit scheme. J Comput Phys 1986;62(1):66–82.
[43] Versteeg HK, Malalasekera W. An introduction to computational fluid dynamics: the finite volume method. Pearson education; 2007.
[44] Vinuesa R, Noorani A, Lozano-Durán A, Khoury GKE, Schlatter P, Fischer PF, Nagib HM. Aspect ratio effects in turbulent duct flows studied through direct numerical simulation. J Turbul 2014;15(10):677–706.
[45] Kushwaha A, Park JS, Graham MD. Temporal and spatial intermittencies within channel flow turbulence near transition. Phys Rev Fluids 2017;2:024603. http://dx.doi.org/10.1103/PhysRevFluids.2.024603, URL: https://link.aps.org/doi/10.1103/PhysRevFluids.2.024603.
[46] Agrawal R, Ng HC-H, Davis EA, Park JS, Graham MD, Dennis DJ, Poole RJ. Low-and high-drag intermittencies in turbulent channel flows. Entropy 2020;22(10):1126.
[47] Jones J. An improvement in the calculation of turbulent friction in rectangular ducts. J Fluids Eng 1976;98(2):173–80. http://dx.doi.org/10.1115/1.3448250.
[48] Shahmardi A, Zade S, Ardekani MN, Poole RJ, Lundell F, Rosti ME, Brandt L. Turbulent duct flow with polymers. J Fluid Mech 2019;859:1057–83.
[49] Pope SB. Turbulent flows. 2001.
[50] Keirsbulck L, Labraga L, Gad-el Hak M. Statistical properties of wall shear stress fluctuations in turbulent channel flows. Int J Heat Fluid Flow 2012;37:1–8.